CHEMISTRY OF MATERIALS
Cite This: Chem. Mater. 2019, 31, 7565−7573
Article
pubs.acs.org/cm

Dendrite-Free and Stable Lithium Metal Anodes Enabled by an Antimony-Based Lithiophilic Interphase

Tao Chen,[†] Weihua Kong,[†] Peiyang Zhao,[†] Huinan Lin,[†] Yi Hu,[†] Renpeng Chen,[†] Wen Yan,[†] and Zhong Jin*[,†,‡]

[†]Key Laboratory of Mesoscopic Chemistry of MOE, Jiangsu Key Laboratory of Advanced Organic Materials, School of Chemistry and Chemical Engineering, Nanjing University, Nanjing 210023, China

[‡]Shenzhen Research Institute of Nanjing University, Shenzhen 518063, China

Supporting Information

ABSTRACT: Rechargeable lithium metal batteries are of tremendous interest due to the high theoretical capacity and low reduction potential of lithium metal anode. However, the formation of unstable solid electrolyte interphase (SEI) results in lithium dendrite growth and low Coulombic efficiency during Li plating/stripping processes. Herein, we report an effective strategy to stabilize Li metal anode by in situ constructing antimony-based lithiophilic interphase on Li anode (Sb−Li) using antimony triiodide-tetrahydrofuran (THF) solution. The antimony-based lithiophilic interphase is composed of amorphous antimony and lithium compounds, revealed by in-depth X-ray photoelectron spectroscopy. The Sb−Li anode enables dendrite-free Li deposition in both ether- and ester-based electrolytes. As a result, as-assembled lithium−sulfur (Li−S) batteries with Sb−Li anode exhibit an initial capacity of 915 mAh g^{-1} at 1.0 C and a capacity retention >83% after 400 cycles. *Operando* Raman analysis confirmed that the antimony-based lithiophilic interphase can prevent parasitic side reactions, and also relieve the shuttle effect of polysulfides. Furthermore, Sb−Li|LiFePO$_4$ cells have also realized high rate performance and stable cyclability. We expect this effective strategy for stabilizing Li metal anode will provide a valuable route to develop high-energy Li metal batteries.

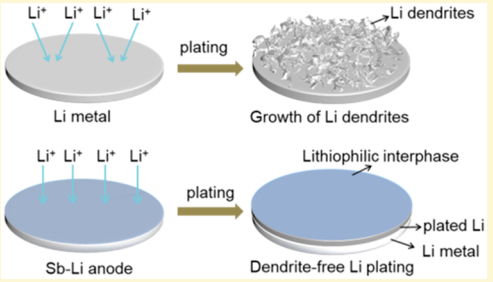

INTRODUCTION

Recently, the ever-increasing demands of portable electronic devices and electrical vehicles have greatly promoted the research interests in high-energy rechargeable batteries.[1,2] Lithium (Li) metal is regarded as a promising anode material for next-generation rechargeable batteries owing to its highest theoretical capacity (3860 mAh g^{-1}) and most negative redox potential (−3.04 V vs standard hydrogen electrode) among all metals.[3,4] However, unlike conventional graphite anode, nonuniform deposition of Li and its high reactivity with the electrolyte lead to uncontrolled formation of fragile solid-electrolyte interphase (SEI) and needle-like dendrites, which may cause serious safety issues.[5−7] Meanwhile, during repeated Li plating/stripping, the accumulated SEI continually consumes electrolyte and Li, leading to low Coulombic efficiency, increased interfacial resistance, and limited cycle life.[8−10] The mechanical instability and inhomogeneity of the SEI layer has become a big bottleneck for the commercialization of secondary batteries based on lithium metal anodes.

To date, a number of strategies have been proposed to construct stable electrode/electrolyte interphase for suppressing the Li dendrite growth and reduce side/parasitic reactions. High-concentration lithium salts[11] and different electrolyte additives (polysulfides,[12] $LiNO_3$,[13] organosulfides,[14] nanodiamonds[15]) have been utilized to form stable SEI layers for stabilizing the Li metal surface. However, owing to the continuous consumption of the additives or salts upon cycling, achieving long-term suppression of Li dendrite growth is still not fully satisfying. Solid and polymer/gel electrolytes with high mechanical modulus can physically prevent the Li dendrite penetration through the separator.[16−19] Nevertheless, the high interfacial resistance and low room-temperature conductivity of these electrolytes greatly restrict their practical utilization. Different from the above two methods, constructing a stable and robust interfacial protective layer is another feasible route to stabilize the Li plating/stripping processes of lithium metal anode. Recently, artificial SEI (such as Al_2O_3,[20,21] lithium phosphorus oxynitride (LiPON),[22] $LiPO_3$,[23] and Li_3N[24]), Li-rich alloys ($Li_{13}In_3$[25] and lithium silicide[26]), and carbon matrix (carbon nanospheres,[5] multiwall carbon nanotubes,[27] graphene[28]) have been proved to be effective for regulating Li deposition and blocking Li dendrite growth to varying extent. Briefly, we suggest that an ideal protective layer should possess the following features: (1) high ionic conductivity for fast Li ion transport,[29,30] (2) electronic insulation/low electronic conductivity for inhibiting electrolyte decomposition,[25,31] (3) good mechanical strength to prevent dendrite penetration,[32] and (4) high chemical stability to

Received: June 16, 2019
Revised: August 20, 2019
Published: August 20, 2019

DOI: 10.1021/acs.chemmater.9b02356
Chem. Mater. 2019, 31, 7565−7573

endure long-term cycling processes.[33] Therefore, new approaches to rationally fabricate a highly stable SEI that can effectively prevent the electrolyte loss and dendrite growth are urgently required for the practical application of lithium metal batteries.

To fulfill the above requirements, here we report an effective strategy for controlled formation of a multifunctional antimony-based lithiophilic interphase on Li metal anode. Antimony, as a potential candidate of anode materials for Li-ion batteries,[34] can react with Li metal to form a layer of Li_3Sb alloy, which has low interfacial resistance to enable fast lithium ion migration and also can effectively passivate the highly reactive Li anode. By immersing Li electrode in antimony triiodide-THF solution, a lithiophilic interphase with compositional gradients of amorphous antimony species (Li_3Sb, Sb, and SbO_x) and lithium compounds (LiI, LiOH, Li_2CO_3, and Li_2O) can be in situ formed. During electrochemical tests, the antimony-based lithiophilic interphase exhibits high ionic conductivity, low electronic conductivity, and high electrochemical stability, thus it can serve as an effective artificial SEI layer. Moreover, because of the electronic insulation of LiI and other compounds in the lithiophilic interphase,[35] the deposition of Li dendrites on the surface can be inhibited, enabling uniform Li metal deposition underneath the lithiophilic interphase.[29] As a result, this antimony-based lithiophilic interphase on Li (Sb−Li) anode can effectively prevent the formation of Li dendrites, reduce the parasitic reactions with liquid electrolyte and render the uniform deposition of Li metal. The symmetric cells based on Sb−Li electrodes show very stable Li plating/stripping voltage profiles for 1300 and 260 h at 0.5 and 2.0 mA cm^{-2}, respectively. Moreover, when paired with sulfur composite or $LiFePO_4$ cathodes, the Sb−Li anode can greatly enhance the cycling stability and rate performance in contrast to pristine Li anode. In particular, the antimony-based lithiophilic interphase can reduce the side reactions of soluble long-chain polysulfides in ether-based electrolytes and greatly inhibit the shuttle effect, thus leading to highly improved performance of Li−S batteries.

EXPERIMENTAL SECTION

Preparation of Antimony-Protected Lithium Anodes. An in situ formed antimony-based lithiophilic interphase was coated on lithium foil by a simple displacement reaction process between Li metal and SbI_3 at room temperature. Typically, lithium foil (with the diameter of ∼12 mm and the thickness of ∼500 μm) was polished using plastic scraper in an argon-filled glovebox (<1 ppm oxygen and H_2O). Subsequently, the polished lithium foil were immersed in a 50 mM SbI_3-tetrahydrofuran(THF) solution (5 mL) for about 3 min until the surface was completely turned to black. The Sb−Li electrode was rinsed with THF solvent to remove residual SbI_3, and preserved in the glovebox prior to use. As control samples, lithium foils were also immersed in 5, 25, or 100 mM SbI_3-THF solutions for the same period to adjust the surface morphologies of the antimony-based lithiophilic interphase.

Preparation of CNTs/S Composite Cathodes. The CNTs/S cathodes were prepared via a melt-diffusion strategy. Briefly, commercial CNTs were ground together with sulfur powder at a weight ratio of 3:7, and then the mixture was coheated at 155 °C in a sealed glass vessel for 6 h to yield CNTs/S composite with 67 wt % sulfur content. A slurry was prepared by mixing 80 wt % of as-prepared CNTs/S composite, 10 wt % of KJ-black (EC600J) as conductive agent, and 10 wt % of polyvinylidene fluoride (PVDF) in *N*-methyl-2-pyrrolidone (NMP). The slurry was then casted on Al foil and dried in a vacuum oven at 55 °C for 12 h. The CNTs/S electrodes were cut into disks with a diameter of 12 mm, and then transferred into the glovebox. The areal mass loading of sulfur in the electrodes was normally 1.1 mg cm^{-2} and increased to 2.8 or 4.8 mg cm^{-2} for the thick electrodes.

Preparation of LiFePO4 Cathodes. Briefly, 80 wt % of commercial $LiFePO_4$ powder, 10 wt % of super P carbon black, 10 wt % of PVDF was mixed in NMP solvent to form a slurry. The slurry was blade-coated on Al foil and dried in a vacuum oven at 100 °C for 12 h. Then, the electrode was cut into small disks with a diameter of 12 mm. The areal loading of $LiFePO_4$ was about 2.5−3.0 mg cm^{-2}.

Materials Characterizations. The top-view and side-view morphologies of the antimony-based lithiophilic interphase on lithium foil were observed on scanning electron microscope (SEM, FEI Nova-450 V). To avoid possible surface oxidation and parasitic reactions, the samples were placed in a sealed vial filled with argon and quickly transferred from glovebox to the high-vacuum chamber. Energy-dispersive X-ray spectrometer (EDX, Bruker Quantax-200) attached on the SEM was used to analyze the compositions. To observe the electrode morphologies after cycling, the cycled cells were dissembled inside the glovebox, and the cycled Li anodes were rinsed with DME and dried in the glovebox at room temperature. Raman spectra were collected using a Horiba JY Evolution Raman spectrometer with an excitation laser of 473 nm wavelength. X-ray photoelectron spectroscopy (XPS) were performed on a PHI-5000 VersaProbe X-ray photoelectron spectrometer with an Al Kα X-ray radiation to investigate the surface compositions, and the depth-profiles of XPS analysis were obtained with the assistance of argon-ion sputtering for 3 or 7 min. The samples were quickly transferred from glovebox to the XPS chamber with the help of an Ar-filled sealed vial to avoid surface oxidation. The sulfur content in the CNTs/S composite was determined by thermogravimetric analysis (STA 449C, NETZSCH) under N_2 with a ramp rate of 10 °C min^{-1}.

Electrochemical Measurements. Electrochemical tests were all carried out using CR2032 coin cells. The symmetric cells were assembled with two pristine Li or Sb−Li electrodes, a Celgard 2400 polypropylene separator, and 30 μL of 1.0 M lithium bis-(trifluoromethane)sulfonimide LiTFSI in 1,3-dioxolane/1,2-dimethoxyethane (DOL/DME; 1:1 vol) as the electrolyte. To evaluate the performances of the protected layer in full cells, pristine Li and Sb−Li electrodes were used to assemble Li−S and $LiFePO_4$ full cells with CNTs/S and $LiFePO_4$ cathodes, respectively. The Li−S cells were assembled by using CNTs/S cathodes, Celgard 2400 separators, pristine Li or Sb−Li anodes. The electrolyte was 30 μL of 1.0 M LiTFSI in DOL/DME (1:1 vol %) added in each Li−S cell. The $LiFePO_4$ full cells were assembled with $LiFePO_4$ cathodes, Celgard 2400 separators and pristine or Sb−Li Li anodes. Then, 40 μL of 1 M $LiPF_6$ in ethylene carbonate/diethyl carbonate (EC/DEC, 1:1 vol %) was used as the electrolyte for the $LiFePO_4$ full cells. All coin cells were galvanostatically cycled on a LAND-CT2001 8-channel battery tester. The voltage windows for the tests of CNTs/S and $LiFePO_4$ cathodes were set to 1.8−2.8 and 2.5−4.25 V, respectively. Electrochemical impedance spectroscopy (EIS) measurements were conducted on a Chenhua CHI-760E electrochemical workstation between a frequency range of 100 kHz to 0.1 Hz. The ionic conductivity (σ) of the antimony-based lithiophilic interphase was calculated based on the equation: $\sigma = d/SR$, where d (cm) is the thickness of the electrode, S (cm^2) is the contact area of the electrode, and R (Ω) is the interfacial resistance.

***Operando* Raman Spectroscopic Analysis.** The electrochemical cell with a sealed quartz widow of 5 mm diameter for *operando* Raman analysis was purchased from Beijing Scistar Technology Co. Ltd. For the collection of *operando* Raman spectra on the cathodic side, self-supporting carbon paper was used as the sulfur host material. To reduce the signal-to-noise ratio and enhance the peak intensities of Raman spectra, the areal sulfur loading of the cathodes was set to ∼3.0 mg cm^{-2}. The Li−S cells were galvanostatically discharged at a current density of 0.2 C at room temperature. Meanwhile, the *operando* Raman spectra were recorded on a Horiba JY Evolution Raman spectrometer with an excitation laser of 473 nm wavelength and L50× objective lens.

DOI: 10.1021/acs.chemmater.9b02356
Chem. Mater. 2019, 31, 7565−7573

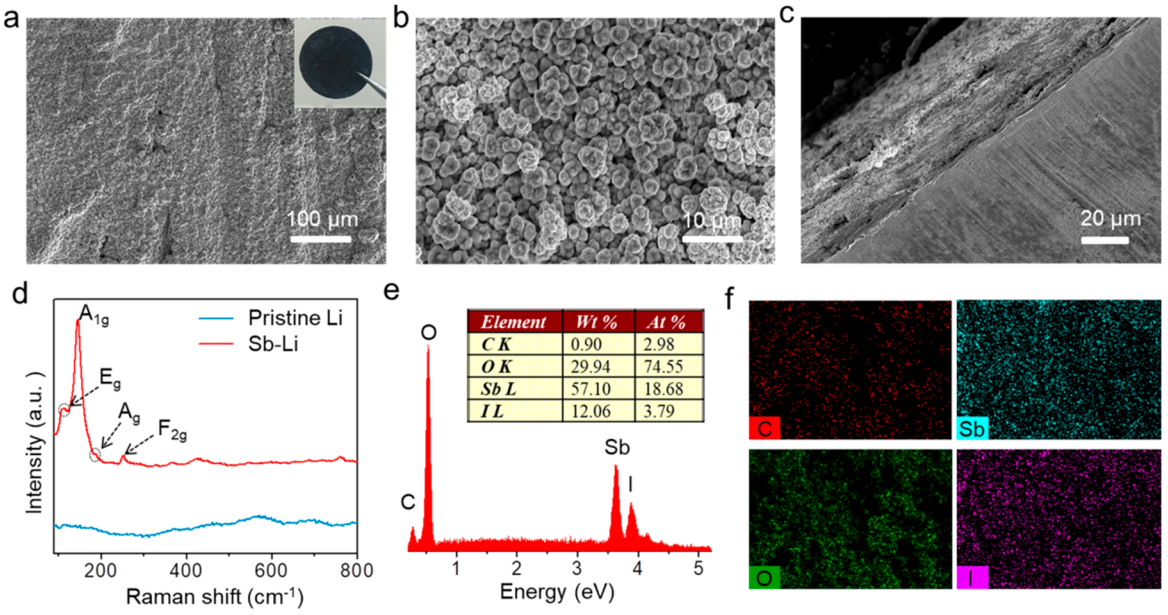

Figure 1. Structure and composition characterizations of antimony-based lithiophilic interphase. (a and b) Top-view SEM images of antimony-based lithiophilic interphase covered on Li metal. The inset in panel a shows a digital image of the Li foil coated with antimony-based lithiophilic interphase. (c) Cross-section SEM image of antimony-based interfacial layer protected Li foil. (d) Raman spectra of pristine Li foil and antimony-based interfacial layer protected Li foil. (e and f) EDX spectrum and corresponding element mappings of antimony-based lithiophilic interphase.

RESULTS AND DISCUSSION

The antimony-based lithiophilic interphase was prepared by the spontaneous reaction of Li metal and antimony triiodide (SbI_3) in the anhydrous THF solvent at room temperature. First, to remove any possible oxidization layer or contaminations, the Li metal foil was placed in an Ar-filled glovebox and polished until the surface showed silvery luster. The polished Li metal was then immersed into 50 mM SbI_3/THF solution for a few minutes to form antimony-based lithiophilic interphase on its surface. The surface morphology of the lithiophilic interphase was monitored by scanning electron microscopy (SEM), as shown in Figure 1a,b. The as-obtained lithiophilic interphase on the Li metal surface shows a dense and uniform surface covered with granular structures of about 150−300 nm diameter (Figure 1b). The cross-section view reveals that the thickness of the lithiophilic interphase is ∼2.5 μm (Figure 1c and S1). The formation of the antimony-based lithiophilic interphase was verified by Raman spectroscopy (Figure 1d). Two main peaks of E_g and A_{1g} located at 112.3 and 145.3 cm^{-1} show a slight blue shift compared with those of metallic antimony in previous literature,[36,37] which might result from partly alloyed antimony and amorphous Li_3Sb (Figure S2). The additional A_g band (255.3 cm^{-1}) and F_{2g} band (189.7 cm^{-1}) can be assigned to SbO_x, which should be originated from the surface oxidation during the transfer process of samples.[37] Energy dispersive X-ray spectroscopy (EDS) analysis and corresponding elemental mappings of the antimony-based lithiophilic interphase show the uniform distribution of Sb, C, O, and I elements (Figure 1e,f). The iodine is presented in the form of lithium iodide (LiI), which accounts for a weight ratio of 12.7 wt % in the antimony-based lithiophilic interphase. Moreover, the effects of reagent concentration on the surface morphology of the lithiophilic interphase were also investigated. It was found that SbI_3/THF solutions with lower concentrations (5 or 25 mM) could not form a compact and dense lithiophilic interphase on the Li surface (Figure S3a,b). At higher SbI_3 concentration (100 mM), rough surface with some cracks was observed (Figure S3c), which may lead to uneven Li deposition.

The compositions and chemical states of antimony-based lithiophilic interphase were further probed by X-ray photoelectron spectroscopy (XPS) profile analysis (Figure 2). The content of oxygen dramatically decreased after Ar-ion

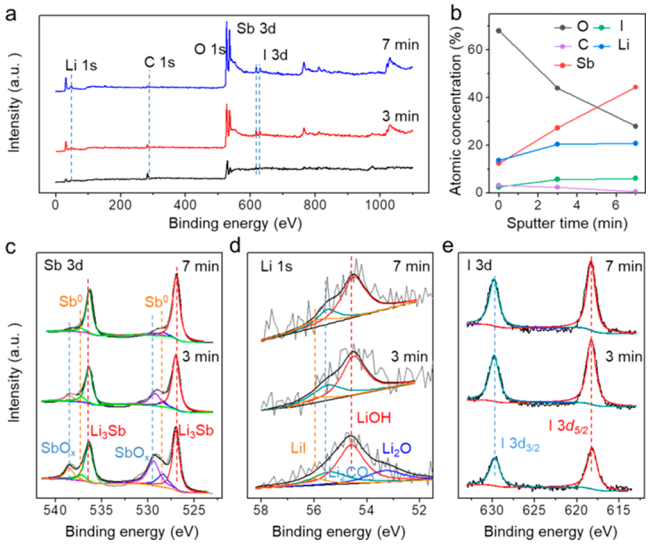

Figure 2. In-depth XPS analysis of antimony-based lithiophilic interphase. (a) XPS spectra of antimony-based lithiophilic interphase at pristine state, after Ar-ion bombardment for 3 min, and after Ar-ion bombardment for 7 min, respectively. (b) The depth profiles of atomic concentrations of O, Li, Sb, I, and C elements in the antimony-based lithiophilic interphase. (c−e) High-resolution XPS depth profiles at (c) Sb 3d, (d) Li 1s, and (e) I 3d regions of antimony-based lithiophilic interphase at pristine state, after Ar-ion bombardment for 3 min, and after Ar-ion bombardment for 7 min, respectively.

DOI: 10.1021/acs.chemmater.9b02356
Chem. Mater. 2019, 31, 7565−7573

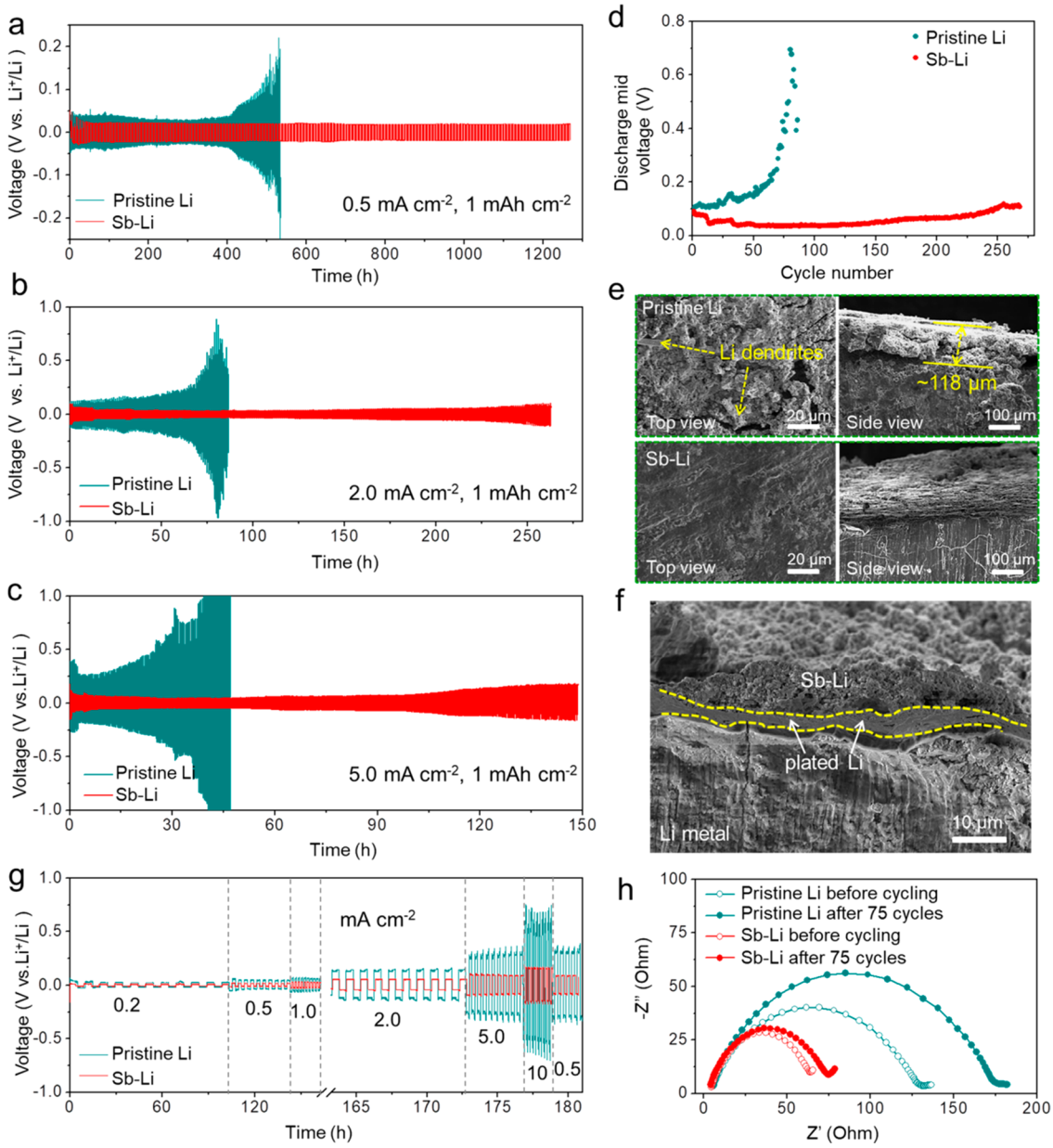

Figure 3. Cycling stability comparisons of pristine Li and Sb−Li electrodes. (a−c) Voltage profiles of the symmetric cells with pristine Li and Sb−Li electrodes under the current densities of (a) 0.5, (b) 2.0, and (c) 5.0 mA cm^{-2} with a fixed capacity of 1 mA h cm^{-2}, respectively. (d) Discharge mid voltage differences of the symmetric cells with pristine Li and Sb−Li electrodes corresponding to panel b. (e) Morphologies of pristine Li and Sb−Li electrodes after cycling at a current density of 2.0 mA cm^{-2} for 75 h. (f) The cross-sectional image of Sb−Li electrode after plating at 2.0 mAh cm^{-2}. (g) Rate performance test of symmetric cells with pristine Li and Sb−Li electrodes at different current densities of 0.2 0.5, 1.0, 2.0, 5.0, and 10 mA cm^{-2} with a fixed capacity of 1 mAh cm^{-2}. (h) Electrochemical impedance spectra of the symmetric cells with pristine Li and Sb−Li electrodes before and after cycling at 2.0 mA cm^{-2} for 75 cycles.

sputtering (Figure 2b), suggesting that the surface oxide layer mainly existed on the upper 30 nm.[25] The high-resolution Sb 3d XPS spectrum of Sb−Li electrode exhibits two main peaks at 526.9 and 536.4 eV (Figure 2c, bottom), which are assigned to Li_3Sb.[38] The adjacent peaks at 528.4 and 537.2 eV corresponded to zerovalent Sb metal.[39] Besides, two weak peaks of SbO_x at 529.4 and 538.5 eV are also observed.[40] Though the bombardment of Ar-ion sputtering, the antimony-based lithiophilic interphase can be etched by different thicknesses for accurate depth profiling.[25,32] With the time of Ar-ion bombardment increased from 3 to 7 min, the peaks related to Sb metal and SbO_x species gradually disappeared (Figure 2c), while the peaks of Li_3Sb metal showed no obvious change. The Li 1s XPS spectrum can be deconvoluted into four peaks at 55.9, 55.4, 54.5, and 53.5 eV (Figure 2d, bottom), which can be assigned to LiI, Li_2CO_3, LiOH, and Li_2O, respectively.[41] However, after 3 min of Ar-ion bombardment, the characteristic peak of Li_2O in the lithiophilic interphase was disappeared (Figure 2d, center), indicating that the antimony-based lithiophilic interphase can prevent the Li metal from further oxidation. In the I 3d XPS spectrum, two deconvoluted peaks of I $3d_{5/2}$ and $3d_{3/2}$ bands corresponding to LiI are observed at 618.3 and 629.9 eV, respectively (Figure 2e).[42] It can be concluded that the main ingredients in the antimony-based lithiophilic interphase are amorphous antimony (Li_3Sb, SbO_x, and Sb) and lithium compounds (LiI,

DOI: 10.1021/acs.chemmater.9b02356
Chem. Mater. 2019, 31, 7565−7573

LiOH, Li_2CO_3, and Li_2O). Note that Li_3Sb and LiI are the major components at the inner region, while SbO_x, Sb, Li_2O, LiOH, and Li_2CO_3 are mainly distributed at the upper surface region.

To evaluate the electrochemical performances of antimony-based lithiophilic interphase, symmetric cells with pristine Li or Sb−Li electrodes were cycled at various current densities (0.5, 2.0, or 5.0 mA cm^{-2}) with a stripping/plating capacity of 1 mAh cm^{-2} using 1.0 M LiTFSI in 1,2-dimethoxyethane/1,3-dioxolane (DME/DOL; 1:1) electrolyte. The symmetric cell based on pristine Li electrodes displayed a gradual increase in voltage hysteresis during Li plating/stripping processes. In contrast, the symmetric cell with Sb−Li electrodes exhibited low voltage polarization during cycling and greatly improved cycling life. At a low current density of 0.5 mA cm^{-2}, the symmetric cell based on pristine Li electrodes exhibited large voltage divergence (100 mV) after 400 h, and followed by short-circuit at 520 h (Figure 3a). On the contrary, the symmetric cell with Sb−Li electrodes presented stable voltage profiles with low hysteresis below 50 mV and a flat plateau over 1268 h. When the current density increased to 2.0 mA cm^{-2}, the symmetric cell based on pristine Li electrodes exhibited a sharp voltage divergence to 340 mV after 50 h and failed quickly after merely 80 h, due to the repeated formation and fracture of resistive SEI at the Li/electrolyte interfaces (Figure 3b). However, the symmetric cell with Sb−Li electrodes cycled at 2.0 mA cm^{-2} still showed good cycling stability for over 260 h (260 cycles) and low voltage hysteresis of ∼70 mV. The differences in cycling stability were more obvious at higher current density. At a high current density of 5.0 mA cm^{-2}, the symmetric cell based on pristine Li electrodes presented continuous increase in voltage hysteresis after only several cycles and resulted in short-circuits after 47 h (Figure 3c). In contrast, the symmetric cell with Sb−Li electrodes can be stably plated/stripped for more than 148 h (370 cycles) with an average voltage hysteresis of ∼200 mV. Compared with the Sb−Li electrode, the pristine Li electrode exhibited a large discharge mid voltage difference of 0.69 V after only 75 cycles at 2.0 mA cm^{-2} (Figure 3d), indicating the failure of the cell caused by unstable SEI and dendrite growth; while the Sb−Li electrode showed stable discharge mid voltage for over 260 cycles. The Nyquist plots and ionic conductivity of the cells with Sb−Li electrodes as a function of temperature are shown in Figure S4. The interfacial resistance of the symmetric cells with Sb−Li anodes gradually decreased with the increase of temperature. The ionic conductivity of the Sb−Li electrodes is measured to be 1.11×10^{-3} S cm^{-1} at 30 °C.

To evaluate the stability of Sb−Li electrode, time-dependent electrochemical impedance spectroscopy (EIS) of Li|Li symmetric cells based on pristine Li or Sb−Li electrodes was measured. As the testing time increases, the charge transfer resistance (R_{ct}) of the cell based on pristine Li electrodes continuously increases, whereas the R_{ct} of the cell with Sb−Li electrodes shows very little change after 50 h (Figure S5). This result demonstrates the high stability of Sb−Li electrode, which can be attributed to its lithiophilic interface with organic electrolyte. The structure and composition evolutions of pristine Li and Sb−Li electrodes after long-term cycling were also compared. Figure 3e shows the morphologies of pristine Li and Sb−Li electrodes after cycling at 2.0 mA cm^{-2} for 75 h. The pristine Li electrode displays uneven and porous surface covered by numerous Li dendrites, and the thickness of loose dendrite structure is measured to be ∼118 μm. By contrast, the Sb−Li electrode shows a flat and dense surface without visible Li dendrite formation. The cross-section SEM image of Sb−Li electrode after plating at 2.0 mAh cm^{-2} shows the uniform deposition of lithium metal under the antimony-based lithiophilic interphase (Figure 3f). Moreover, XPS analysis of Sb−Li electrode were also performed after Li plating/stripping for 10 cycles (Figure S6). The XPS peak intensities and positions showed very slight changes, except that the peaks of Li_3Sb alloy originated from the lithiation of Sb metal was emerged. This result indicates that the antimony-based lithiophilic interphase is electrochemically stable during cycling.

The rate capability of pristine Li and Sb−Li electrodes was evaluated by cycling the symmetric cell at various current densities from 0.5 to 10 mA cm^{-2} with a constant capacity of 1 mAh cm^{-2}. For pristine Li electrode, the voltage hysteresis sharply increased from 150 to 720 mV as the current densities increases from 0.2 to 10 mA cm^{-2}. In comparison, when cycled at 0.2, 0.5, 1.0, 2.0, 5.0, and 10 mA cm^{-2}, the average voltage hysteresis of symmetric cell based on Sb−Li electrodes was around 18, 32, 60, 105, 185, and 370 mV, respectively (Figure 3g). Obviously, the symmetric cell based on Sb−Li electrodes shows much lower voltage hysteresis at high current densities. Electrochemical impedance spectroscopy was also conducted to reveal the variation of interfacial resistance in the symmetric cells before and after cycling. Figure 3h shows the Nyquist plots of symmetric cells with pristine Li and Sb−Li electrodes before and after 75 cycles at 2.0 mA cm^{-2}. The semicircle at the high-frequency range is visually interpreted as the interfacial charge-transfer impedance at the electrolyte/electrode interface. Before cycling, the interfacial resistance of the symmetric cell with pristine Li electrodes was 132 Ω, which increased to a higher resistance of 178 Ω after 75 cycles. In contrast, the interfacial resistance of the symmetric cell based on Sb−Li electrodes only slightly increased from 63 to 74 Ω after 75 cycles. These results verify the improved cycling stability and fast Li stripping/plating kinetics attributed to the antimony-based lithiophilic interphase.

To further demonstrate the effectiveness of antimony-based lithiophilic interphase in carbonate-based electrolytes, galvanostatic plating/stripping tests of symmetric cells based on pristine Li and Sb−Li electrodes using 1.0 M $LiPF_6$−EC/DMC (ethylene carbonate/dimethyl carbonate) electrolyte were also carried out (Figure S7). Compared with pristine Li electrodes, the cell with Sb−Li electrodes exhibits a stable voltage profile with a low hysteresis of ∼75 mV for 500 h, suggesting that the antimony-based lithiophilic interphase can greatly enhance the interfacial stability of Li metal anode in carbonate electrolyte.

Li−S batteries have attracted great attention due to its high theoretic energy density.[43] However, some critical issues associated with Li metal anode, such as Li dendrite growth and its high reactivity to electrolyte/polysulfide intermediates, still remain as major concerns.[44] The antimony-based lithiophilic interphase is expected to avoid the direct contact of Li anode with polysulfide species, thus capable of blocking the side reactions of Li anode and suppressing the shuttle effect of polysulfides.[45−47] To verify the superiority of the Sb−Li anode compared to pristine Li anode, lithium−sulfur (Li−S) batteries using commercial carbon nanotubes (CNTs) as the sulfur host material were assembled and tested (Figure S8a). The melt-diffusion method was used to prepare the CNTs/S cathodes with a sulfur content of 67 wt % (Figure S8b). The

DOI: 10.1021/acs.chemmater.9b02356
Chem. Mater. 2019, 31, 7565−7573

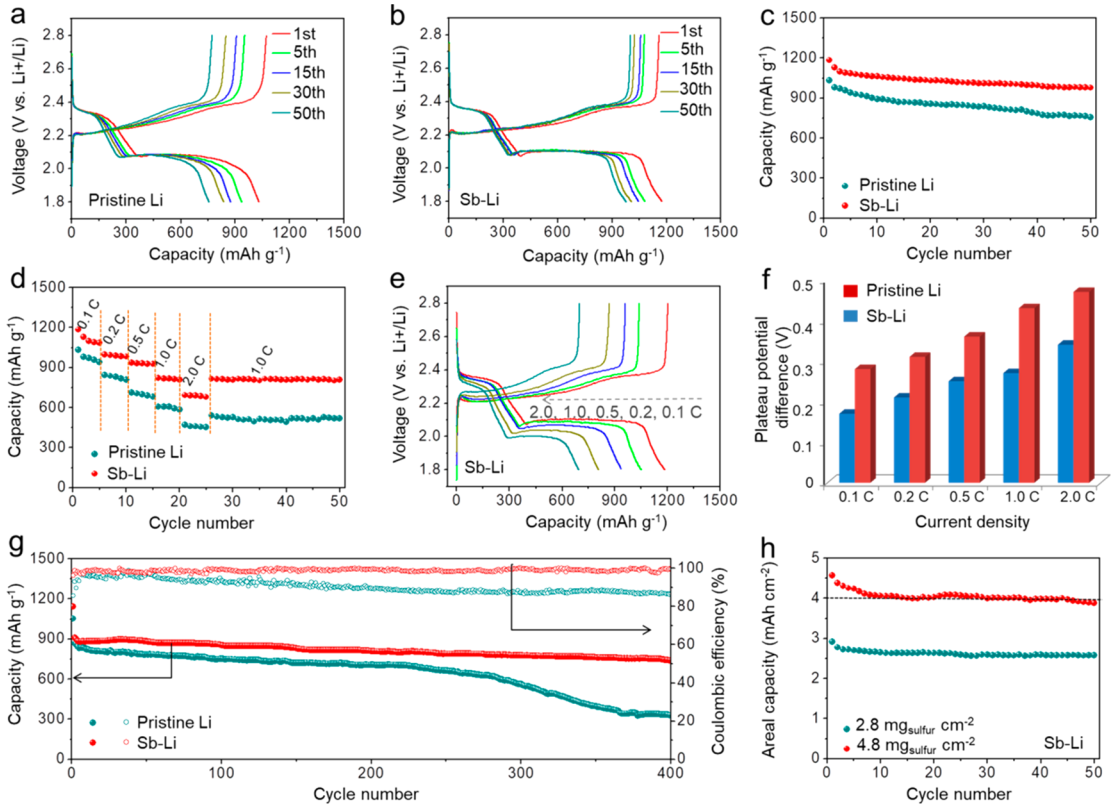

Figure 4. Electrochemical performances of Li−S batteries based on pristine Li and Sb−Li anodes. (a, b) Galvanostatic charge/discharge curves of Li−S batteries using (a) pristine Li and (b) Sb−Li anodes cycled at 0.1 C (1 C = 1675 mA g_{sulfur}^{-1}), respectively. (c) Cycling performance of Li−S batteries with pristine Li and Sb−Li anodes at 0.1 C. (d and e) Discharge capacity and voltage profiles of Li−S batteries based on pristine Li and Sb−Li anodes at stepwise current rates from 0.1 to 2.0 C, respectively. (f) The potential differences between the charge and discharge plateaus at various current rates of Li−S batteries with pristine Li and Sb−Li anodes. (g) Long-term cycling performances of Li−S batteries with pristine Li and Sb−Li anodes at 1.0 C. (h) The areal capacities of Li−S batteries using Sb−Li anodes with high areal mass loadings of CNTs/S cathodes (2.8 and 4.8 mg_{sulfur} cm^{-2}) cycled at 0.1 C.

galvanostatic charge/discharge behaviors of the Li−S cells based on pristine Li and Sb−Li anodes at current density of 0.1 C were investigated (Figure 4a−c). As shown in Figure 4a, the discharge curves of the cell with pristine Li anode exhibited two voltage plateaus at around 2.3 and 2.1 V at a current density of 0.1 C, which is consistent with the multistep sulfur electro-reduction in ether-based electrolyte. The discharge and charge plateaus of both Li−S cells with pristine Li and Sb−Li electrodes during the first cycle are consistent with the cathodic and anodic peak positions in the corresponding cyclic voltammetry curves (Figure S9). Note that the Li−S cell with Sb−Li anode shows lower potential hysteresis and higher discharge capacity than that of the Li−S cells based on pristine Li anode (Figure 4b). Figure 4c shows the cycling performances of the Li−S cells based on pristine Li and Sb−Li anodes. After 50 cycles at 0.1 C, the discharge capacity of the cell with Sb−Li anode maintained at 1185 mA h g^{-1} with a capacity retention as high as 90%, suggesting that the Sb−Li anode can effectively block the shuttle effect of polysulfides; while the cell with pristine Li anode retained only 74% of its initial discharge capacity.

The rate performances of Li−S batteries based on pristine Li and Sb−Li anodes were evaluated at various current densities (Figure 4d). The discharge capacities of the cell with Sb−Li anode were 1120, 991, 933, 818, and 688 mAh g^{-1} at different current densities of 0.1, 0.2, 0.5, 1.0, and 2.0 C, respectively. When the current rate recovered back to 1.0 C, the cell still delivered a high discharge capacity of 815 mAh g^{-1}. In contrast, the cell with pristine Li anode showed significantly lower discharge capacities at high current rates. The superior rate performance of Sb−Li anode should be originated from the lower polarization and better reaction kinetics than pristine Li anode, which was confirmed by the smaller potential differences between the charge/discharge plateaus of Sb−Li anode (Figures 4e,f and S10). The Sb−Li anode also showed good prolonged cycling performance at 1.0 C (Figure 4g). After the activation at 0.1 C for the first cycle, the Li−S cell with Sb−Li anode delivered an initial discharge capacity of 915 mAh g^{-1} at 1.0 C. After 400 cycles, the reversible discharge capacity still maintained at 740 mAh g^{-1}. The capacity retention was up to 80.8%, with an average capacity decay of only 0.05% per cycle. Comparatively, the discharge capacity of the Li−S cell with pristine Li anode accounts for only 37.8% of the initialcapacity (868 mAh g^{-1}) after 400 cycles at 1.0 C. The surface of Sb−Li anode after cycling in a Li−S cell for 400 times at 1.0 C exhibits flat and dendrite-free morphology, whereas clear mossy-like dendrites and cracks are observed on the surface of pristine Li anode after long-term cycling (Figure S11). The areal capacity of Li−S batteries using Sb−Li anodes with higher sulfur loading was also investigated. As shown in Figure 4h, the Li−S batteries with a sulfur loading of 2.8 mg cm^{-2} exhibited an areal capacity of 2.5 mA h cm^{-2} at 0.1 C. When the sulfur loading is further increased to 4.8 mg cm^{-2}, a higher areal capacity of approximate 4.0 mA h cm^{-2} is achieved

DOI: 10.1021/acs.chemmater.9b02356
Chem. Mater. 2019, 31, 7565−7573

after 50 cycles. The competitive battery performances at high sulfur loading demonstrates the promising potential of Sb−Li anodes for the application in high energy-density Li−S batteries.

Operando Raman spectroscopy was conducted to further monitor the chemical evolution of active species during the discharge process, and the apparatus configuration is illustrated in Figure 5a,b. Figure 5c,d show the operando Raman spectra

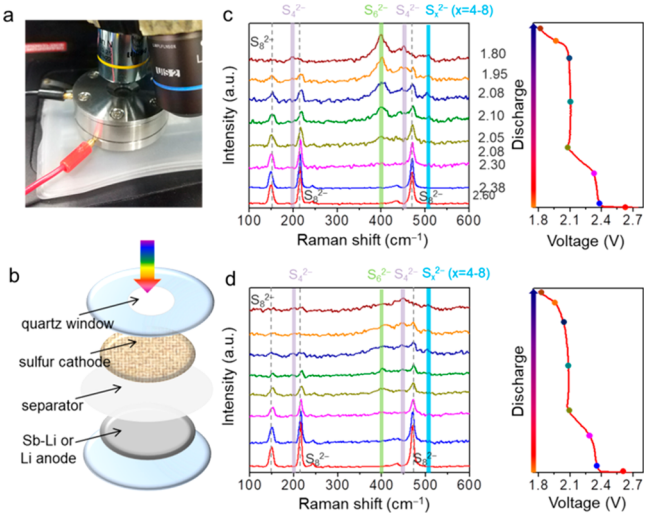

Figure 5. *Operando* Raman spectroscopy analysis. (a) Digital photo of the apparatus for operando Raman analysis performed on a cell equipped with a sealed quartz widow to monitor the chemical evolution of lithium polysulfides during the discharge process. (b) Schematic configuration of the Li−S cells constructed for operando Raman analysis. (c and d) *Operando* Raman spectra of the Li−S cells with pristine Li (c) and Sb−Li (d) anodes at different discharge states.

of the Li−S cells with pristine Li and Sb−Li anodes measured during the first discharge process at 0.2 C, respectively. For the cell with pristine Li anode (Figure 5c), at the initial state, the characteristic Raman peaks at 150, 219, and 479 cm^{-1} are assigned to the formation of long-chain lithium polysulfides (Li_2S_8).[48] During the following discharge process, the peaks corresponding to S_8 gradually weakened and finally diminished, owing to the conversion of long-chain Li_2S_8 to short-chain Li_2S_4 and Li_2S_6. This can be confirmed by the emergence of new Raman peaks at 198, 398, and 450 cm^{-1}.[49,50] At the end of the discharge process, the characteristic peaks of Li_2S_4 and Li_2S_6 were observed, due to the dissolution and shuttle effect of polysulfides. Additionally, no Raman peaks of Li_2S/Li_2S_2 were visible at the end of discharge process, because they mostly existed in the amorphous form.[51] In contrast, for the Li−S cell with Sb−Li anode (Figure 5d), the characteristic peak of Li_2S_6 was barely detectable during the entire discharge process, and the weak peaks of Li_2S_4 only appeared at the fully discharged state. This result demonstrates that the antimony-based protective barrier can effectively alleviate the shuttle effect of polysulfides, in addition to preventing Li dendrite growth and parasitic side reactions.

To further investigate the performance of Sb−Li anode in carbonate-based electrolyte, Li|LiFePO$_4$ and Sb−Li|LiFePO$_4$ cells were assembled using the electrolyte of 1 M $LiPF_6$ in EC-DMC (V%, 1:1). The $LiFePO_4$ cells were first cycled at stepwise current rates for 60 cycles and then cycled at 1.0 C for the subsequent 240 cycles (Figure 6a). The Sb−Li|LiFePO$_4$ cell delivered reversible capacities of ∼141, 135, 117, 105, and

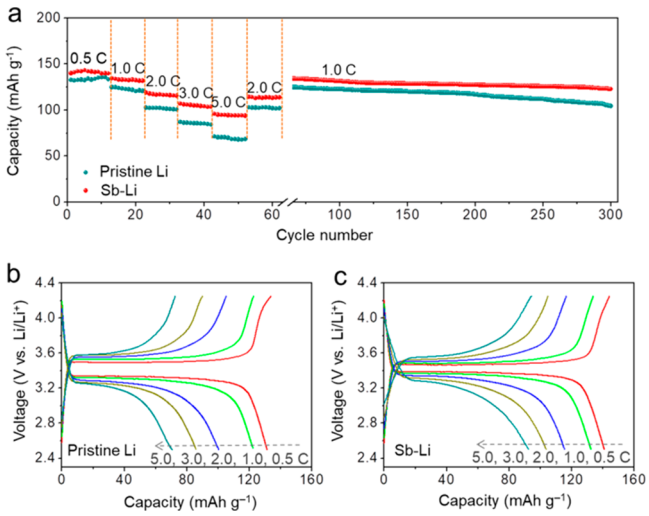

Figure 6. Electrochemical performances of Sb−Li|LiFePO$_4$ and Li|LiFePO$_4$ cells. (a) Rate and cycling performance of Li|LiFePO$_4$ and Sb−Li|LiFePO$_4$ cells. (b and c) Voltage profiles of (b) Li|LiFePO$_4$ and (c) Sb−Li|LiFePO$_4$ cells cycled at stepwise current rates from 0.5 to 5.0 C (1.0 C = 170 mA g^{-1}).

94 mAh g^{-1} at 0.5, 1.0, 2.0, 3.0, and 5.0 C, respectively. Obviously, the rate capabilities of the Sb−Li|LiFePO$_4$ cell are much better than the Li|LiFePO$_4$ cell, especially at high current densities. Moreover, the Sb−Li|LiFePO$_4$ cell exhibited much lower polarization voltages than those of Li|LiFePO$_4$ cell at different current rates (Figure 6b,c), indicating more uniform lithium deposition on Sb−Li anode. After the stepwise rate tests, the LiFePO$_4$ cells were cycled at 1.0 C for the subsequent 240 cycles. The Sb−Li|LiFePO$_4$ cell also showed superior cycling stability in comparison with Li|LiFePO$_4$ cell. Notably, the Sb−Li|LiFePO$_4$ cell exhibited higher capacity retention of 93.1% than that of Li|LiFePO$_4$ cell (83.2%) after the whole cycling process (Figure 6a).

CONCLUSIONS

In summary, here we report a very facile approach for realizing dendrite-free Li plating by the in situ formation of a antimony-based protected layer on Li metal anode. The antimony-based lithiophilic interphase is mainly composed of the compositional gradients of ion-conducting amorphous antimony species (Li_3Sb, Sb, and SbO_x) and electron-insulating LiI components, together with small amounts of Li_2O, LiOH, and Li_2CO_3. This lithiophilic interphase is electrochemically stable in both ether- and ester-based electrolytes. Stable and dendrite-free Li plating/stripping was demonstrated in Sb−Li|Sb-Li symmetric cells. Moreover, the Li−S batteries with Sb−Li anodes exhibited much better rate performance and cycling stability than those with pristine Li anodes. When paired with $LiFePO_4$ cathode, improved rate capability, longer cycling life and lower polarization voltages can be achieved by Sb−Li anode. We hope this work may provide new insights for the suppression of dendrite growth in Li-metal based rechargeable batteries by the construction of artificial lithiophilic interphases.

DOI: 10.1021/acs.chemmater.9b02356
Chem. Mater. 2019, 31, 7565−7573

■ ASSOCIATED CONTENT

Supporting Information

The Supporting Information is available free of charge on the ACS Publications website at DOI: 10.1021/acs.chemmater.9b02356.

Experimental details, scanning electron microscopy and scanning transmission electron microscopy images, X-ray absorption spectroscopy data, X-ray photoelectron spectroscopy data, and other electrochemical data (PDF)

■ AUTHOR INFORMATION

Corresponding Author

*E-mail: zhongjin@nju.edu.cn.

ORCID

Tao Chen: 0000-0003-2536-4145

Zhong Jin: 0000-0001-8860-8579

Author Contributions

The manuscript was written through contributions of all authors. All authors have given approval to the final version of the manuscript.

Notes

The authors declare no competing financial interest.

■ ACKNOWLEDGMENTS

This work was supported by National Key R&D Program of China (2015CB659300, 2016YFB0700600, and 2017YFA0208200), Projects of NSFC (21872069, 51761135104, and 21573108), Natural Science Foundation of Jiangsu Province (BK20180008 and BK20170644), High-Level Entrepreneurial and Innovative Talents Program of Jiangsu Province, and the Fundamental Research Funds for the Central Universities.

■ REFERENCES

(1) Tarascon, J.-M.; Armand, M. Issues and Challenges Facing Rechargeable Batteries. *Nature* **2001**, *414*, 359−369.

(2) Bruce, P. G.; Freunberger, S. A.; Hardwick, L. J.; Tarascon, J. M. Li-O_2 and Li-S Batteries with High Energy Storage. *Nat. Mater.* **2012**, *11*, 19−29.

(3) Tikekar, M. D.; Choudhury, S.; Tu, Z.; Archer, L. A. Design Principles for Electrolytes and Interfaces for Stable Lithium Metal Batteries. *Nat. Energy* **2016**, *1*, 16114.

(4) Lin, D. C.; Liu, Y. Y.; Cui, Y. Reviving the Lithium Metal Anode for High-Energy Batteries. *Nat. Nanotechnol.* **2017**, *12*, 194−206.

(5) Zheng, G.; Lee, S. W.; Liang, Z.; Lee, H.-W.; Yan, K.; Yao, H.; Wang, H.; Li, W.; Chu, S.; Cui, Y. Interconnected Hollow Carbon Nanospheres for Stable Lithium Metal Anodes. *Nat. Nanotechnol.* **2014**, *9*, 618−623.

(6) Xu, W.; Wang, J. L.; Ding, F.; Chen, X. L.; Nasybutin, E.; Zhang, Y. H.; Zhang, J. G. Lithium Metal Anodes for Rechargeable Batteries. *Energy Environ. Sci.* **2014**, *7*, 513−537.

(7) Cheng, X. B.; Zhang, R.; Zhao, C. Z.; Zhang, Q. Toward Safe Lithium Metal Anode in Rechargeable Batteries: a Review. *Chem. Rev.* **2017**, *117*, 10403−10473.

(8) Harry, K. J.; Hallinan, D. T.; Parkinson, D. Y.; MacDowell, A. A.; Balsara, N. P. Detection of Subsurface Structures Underneath Dendrites Formed on Cycled Lithium Metal Electrodes. *Nat. Mater.* **2014**, *13*, 69−73.

(9) Lu, Y.; Tu, Z.; Archer, L. A. Stable Lithium Electrodeposition in Liquid and Nanoporous Solid Electrolytes. *Nat. Mater.* **2014**, *13*, 961−969.

(10) Lin, D.; Liu, Y.; Liang, Z.; Lee, H. W.; Sun, J.; Wang, H.; Yan, K.; Xie, J.; Cui, Y. Layered Reduced Graphene Oxide with Nanoscale Interlayer Gaps as a Stable Host for Lithium Metal Anodes. *Nat. Nanotechnol.* **2016**, *11*, 626−632.

(11) Suo, L.; Hu, Y. S.; Li, H.; Armand, M.; Chen, L. A New Class of Solvent-in-Salt Electrolyte for High-Energy Rechargeable Metallic Lithium Batteries. *Nat. Commun.* **2013**, *4*, 2513.

(12) Li, W.; Yao, H.; Yan, K.; Zheng, G.; Liang, Z.; Chiang, Y. M.; Cui, Y. The Synergetic Effect of Lithium Polysulfide and Lithium Nitrate to Prevent Lithium Dendrite Growth. *Nat. Commun.* **2015**, *6*, 7436.

(13) Aurbach, D.; Pollak, E.; Elazari, R.; Salitra, G.; Kelley, C. S.; Affiito, J. On the Surface Chemical Aspects of Very High Energy Density, Rechargeable Li-Sulfur Batteries. *J. Electrochem. Soc.* **2009**, *156*, A694−A702.

(14) Li, G. X.; Gao, Y.; He, X.; Huang, Q. Q.; Chen, S.; Kim, S. H.; Wang, D. H. Organosulfide-Plasticized Solid-Electrolyte Interphase Layer Enables Stable Lithium Metal Anodes for Long-Cycle Lithium-Sulfur Batteries. *Nat. Commun.* **2017**, *8*, 850.

(15) Cheng, X. B.; Zhao, M. Q.; Chen, C.; Pentecost, A.; Maleski, K.; Mathis, T.; Zhang, X. Q.; Zhang, Q.; Jiang, J.; Gogotsi, Y. Nanodiamonds Suppress the Growth of Lithium Dendrites. *Nat. Commun.* **2017**, *8*, 336.

(16) Zhou, W. D.; Wang, S. F.; Li, Y. T.; Xin, S.; Manthiram, A.; Goodenough, J. B. Plating a Dendrite-Free Lithium Anode with a Polymer/Ceramic/Polymer Sandwich Electrolyte. *J. Am. Chem. Soc.* **2016**, *138*, 9385−9388.

(17) Hood, Z. D.; Wang, H.; Pandian, A. S.; Keum, J. K.; Liang, C. Li_2OHCl Crystalline Electrolyte for Stable Metallic Lithium Anodes. *J. Am. Chem. Soc.* **2016**, *138*, 1768−1771.

(18) Bouchet, R.; Maria, S.; Meziane, R.; Aboulaich, A.; Lienafa, L.; Bonnet, J.-P.; Phan, T. N. T.; Bertin, D.; Gigmes, D.; Devaux, D.; Denoyel, R.; Armand, M. Single-Ion BAB Triblock Copolymers as Highly Efficient Electrolytes for Lithium-Metal Batteries. *Nat. Mater.* **2013**, *12*, 452−457.

(19) Khurana, R.; Schaefer, J. L.; Archer, L. A.; Coates, G. W. Suppression of Lithium Dendrite Growth Using Cross-Linked Polyethylene/Poly(ethylene oxide) Electrolytes: a New Approach for Practical Lithium-Metal Polymer Batteries. *J. Am. Chem. Soc.* **2014**, *136*, 7395−7402.

(20) Han, X.; Gong, Y.; Fu, K.; He, X.; Hitz, G. T.; Dai, J.; Pearse, A.; Liu, B.; Wang, H.; Rubloff, G.; Mo, Y.; Thangadurai, V.; Wachsman, E. D.; Hu, L. Negating Interfacial Impedance in Garnet-Based Solid-State Li Metal Batteries. *Nat. Mater.* **2017**, *16*, 572−579.

(21) Kozen, A. C.; Lin, C.; Pearse, A. J.; Schroeder, M. A.; Han, X.; Hu, L.; Lee, S.; Rubloff, G. W.; Noked, M. Next-Generation Lithium Metal Anode Engineering via Atomic Layer Deposition. *ACS Nano* **2015**, *9*, 5884−5892.

(22) Zhou, B.; Guo, L.; Zhang, Y.; Wang, J.; Ma, L.; Zhang, W. H.; Fu, Z.; Peng, Z. A High-Performance Li-O_2 Battery with a Strongly Solvating Hexamethylphosphoramide ELectrolyte and a LiPON-Protected Lithium Anode. *Adv. Mater.* **2017**, *29*, 1701568.

(23) Li, N. W.; Yin, Y. X.; Yang, C. P.; Guo, Y. G. An Artificial Solid Electrolyte Interphase Layer for Stable Lithium Metal Anodes. *Adv. Mater.* **2016**, *28*, 1853−1858.

(24) Liu, Y.; Lin, D.; Yuen, P. Y.; Liu, K.; Xie, J.; Dauskardt, R. H.; Cui, Y. An Artificial Solid Electrolyte Interphase with High Li-ion Conductivity, Mechanical Strength, and Flexibility for Stable Lithium Metal Anodes. *Adv. Mater.* **2017**, *29*, 1605531.

(25) Liang, X.; Pang, Q.; Kochetkov, I. R.; Sempere, M. S.; Huang, H.; Sun, X.; Nazar, L. F. A Facile Surface Chemistry Route to a Stabilized Lithium Metal Anode. *Nat. Energy* **2017**, *2*, 17119−17124.

(26) Tang, W.; Yin, X.; Kang, S.; Chen, Z.; Tian, B.; Teo, S. L.; Wang, X.; Chi, X.; Loh, K. P.; Lee, H.-W.; Zheng, G. W. Lithium Silicide Surface Enrichment: a Solution to Lithium Metal Battery. *Adv. Mater.* **2018**, *30*, 1801745.

(27) Salvatierra, R. V.; López Silva, G. A.; Jalilov, A. S.; Yoon, J.; Wu, G.; Tsai, A.-L.; Tour, J. M. Suppressing Li Metal Dendrites through a Solid Li-ion Backup Layer. *Adv. Mater.* **2018**, *30*, 1803869.

DOI: 10.1021/acs.chemmater.9b02356
Chem. Mater. 2019, 31, 7565−7573

(28) Bai, M. H.; Xie, K. Y.; Yuan, K.; Zhang, K.; Li, N.; Shen, C.; Lai, Y. Q.; Vajtai, R.; Ajayan, P.; Wei, B. Q. A Scalable Approach to Dendrite-Free Lithium Anodes via Spontaneous Reduction of Spray-Coated Graphene Oxide Layers. *Adv. Mater.* **2018**, *30*, 1801213.
(29) Liang, J.; Li, X.; Zhao, Y.; Goncharova, L. V.; Wang, G.; Adair, K. R.; Wang, C.; Li, R.; Zhu, Y.; Qian, Y.; Zhang, L.; Yang, R.; Lu, S.; Sun, X. In Situ Li_3PS_4 Solid-State Electrolyte Protection Layers for Superior Long-Life and High-Rate Lithium-Metal Anodes. *Adv. Mater.* **2018**, *30*, 1804684.
(30) Pang, Q.; Liang, X.; Shyamsunder, A.; Nazar, L. F. An In Vivo Formed Solid Electrolyte Surface Layer Enables Stable Plating of Li Metal. *Joule* **2017**, *1*, 871−886.
(31) Liao, K. M.; Wu, S. C.; Mu, X. W.; Lu, Q.; Han, M.; He, P.; Shao, Z. P.; Zhou, H. S. Developing a "Water-Defendable" and "Dendrite-Free" Lithium-Metal Anode Using a Simple and Promising $GeCl_4$ Pretreatment Method. *Adv. Mater.* **2018**, *30*, 1705711.
(32) Yan, C.; Cheng, X. B.; Yao, Y. X.; Shen, X.; Li, B. Q.; Li, W. J.; Zhang, R.; Huang, J. Q.; Li, H.; Zhang, Q. An Armored Mixed Conductor Interphase on a Dendrite-Free Lithium-Metal Anode. *Adv. Mater.* **2018**, *30*, 1804461.
(33) Tu, Z.; Choudhury, S.; Zachman, M. J.; Wei, S.; Zhang, K.; Kourkoutis, L. F.; Archer, L. A. Fast Ion Transport at Solid-Solid Interfaces in Hybrid Battery Anodes. *Nat. Energy* **2018**, *3*, 310−316.
(34) He, M.; Kravchyk, K.; Walter, M.; Kovalenko, M. V. Monodisperse Antimony Nanocrystals for High-Rate Li-ion and Na-ion Battery Anodes: Nano versus Bulk. *Nano Lett.* **2014**, *14*, 1255−1262.
(35) Han, F. D.; Yue, J.; Zhu, X. Y.; Wang, C. S. Suppressing Li Dendrite Formation in Li_2S-P_2S_5 Solid Electrolyte by LiI Incorporation. *Adv. Energy Mater.* **2018**, *8*, 1703644.
(36) Drewett, N. E.; Aldous, I. M.; Zou, J. L.; Hardwick, L. J. In Situ Raman Spectroscopic Analysis of the Lithiation and Sodiation of Antimony Microparticles. *Electrochim. Acta* **2017**, *247*, 296−305.
(37) Wu, Q. K.; Song, Y. J. The Environmental Stability of Large-Size and Single-Crystalline Antimony Flakes Grown by Chemical Vapor Deposition on SiO_2 Substrates. *Chem. Commun.* **2018**, *54*, 9671−9674.
(38) Hu, M. J.; Jiang, Y. Z.; Sun, W. P.; Wang, H. T.; Jin, C. H.; Yan, M. Reversible Conversion-Alloying of Sb_2O_3 as a High-Capacity, High-Rate, and Durable Anode for Sodium Ion Batteries. *ACS Appl. Mater. Interfaces* **2014**, *6*, 19449−19455.
(39) Martín, F.; Morales, J.; Sánchez, L. Elucidating the Beneficial Effect of Vinylene Carbonate on the Electrochemistry of Antimony Electrodes in Lithium Batteries. *ChemPhysChem* **2008**, *9*, 2610−2617.
(40) Bodenes, L.; Darwiche, A.; Monconduit, L.; Martinez, H. The Solid Electrolyte Interphase a Key Parameter of the High Performance of Sb in Sodium-Ion Batteries: Comparative X-Ray Photoelectron Spectroscopy Study of Sb/Na-Ion and Sb/Li-Ion Batteries. *J. Power Sources* **2015**, *273*, 14−24.
(41) Wu, S. C.; Zhu, K.; Tang, J.; Liao, K. M.; Bai, S. Y.; Yi, J.; Yamauchi, Y.; Ishida, M.; Zhou, H. S. A Long-Life Lithium Ion Oxygen Battery Based on Commercial Silicon Particles as the Anode. *Energy Environ. Sci.* **2016**, *9*, 3262−3271.
(42) Zhao, Q.; Lu, Y. Y.; Zhu, Z. Q.; Tao, Z. L.; Chen, J. Rechargeable Lithium-Iodine Batteries with Iodine/Nanoporous Carbon Cathode. *Nano Lett.* **2015**, *15*, 5982−5987.
(43) Ji, X.; Lee, K. T.; Nazar, L. F. A Highly Ordered Nanostructured Carbon-Sulphur Cathode for Lithium-Sulphur Batteries. *Nat. Mater.* **2009**, *8*, 500−506.
(44) Chen, T.; Zhang, Z. W.; Cheng, B. R.; Chen, R. P.; Hu, Y.; Ma, L. B.; Zhu, G. Y.; Liu, J.; Jin, Z. Self-Templated Formation of Interlaced Carbon Nanotubes Threaded Hollow Co_3S_4 Nanoboxes for High-Rate and Heat-Resistant Lithium-Sulfur Batteries. *J. Am. Chem. Soc.* **2017**, *139*, 12710−12715.
(45) Liu, T. C.; Hu, J. L.; Li, C. L.; Wang, Y. Unusual Conformal Li Plating on Alloyable Nanofiber Frameworks to Enable Dendrite Suppression of Li Metal Anode. *ACS Appl. Energy Mater.* **2019**, *2*, 4379−4388.
(46) Chu, F. L.; Hu, J. L.; Tian, J.; Zhou, X. J.; Li, Z.; Li, C. L. In Situ Plating of Porous Mg Network Layer to Reinforce Anode Dendrite Suppression in Li-Metal Batteries. *ACS Appl. Mater. Interfaces* **2018**, *10*, 12678−12689.
(47) Wu, H.; Wu, Q. P.; Chu, F. L.; Hu, J. L.; Cui, Y. H.; Yan, C. L.; Li, C. L. Sericin Protein as a Conformal Protective Layer to Enable Air-Endurable Li Metal Anodes and High-Rate Li-S Batteries. *J. Power Sources* **2019**, *419*, 72−81.
(48) Lei, T. Y.; Chen, W.; Lv, W. Q.; Huang, J. W.; Zhu, J.; Chu, J. W.; Yan, C. Y.; Wu, C. Y.; Yan, Y. H.; He, W. D.; Xiong, J.; Li, Y. R.; Yan, C. L.; Goodenough, J. B.; Duan, X. F. Inhibiting Polysulfide Shuttling with a Graphene Composite Separator for Highly Robust Lithium-Sulfur Batteries. *Joule* **2018**, *2*, 2091−2104.
(49) Song, Y. Z.; Zhao, W.; Kong, L.; Zhang, L.; Zhu, X. Y.; Shao, Y. L.; Ding, F.; Zhang, Q.; Sun, J. Y.; Liu, Z. F. Synchronous Immobilization and Conversion of Polysulfides on VO_2-VN Binary Host Targeting High Sulfur Loading Li-S Batteries. *Energy Environ. Sci.* **2018**, *11*, 2620−2630.
(50) Chen, W.; Lei, T. Y.; Qian, T.; Lv, W. Q.; He, W. D.; Wu, C. Y.; Liu, X. J.; Liu, J.; Chen, B.; Yan, C. L.; Xiong, J. A New Hydrophilic Binder Enabling Strongly Anchoring Polysulfides for High-Performance Sulfur Electrodes in Lithium-Sulfur Battery. *Adv. Energy Mater.* **2018**, *8*, 1702889.
(51) Huang, S. Z.; Lim, Y. V.; Zhang, X. M.; Wang, Y.; Zheng, Y.; Kong, D. Z.; Ding, M.; Yang, S. Y.; Yang, H. Y. Regulating the Polysulfide Redox Conversion by Iron Phosphide Nanocrystals for High-Rate and Ultrastable Lithium-Sulfur Battery. *Nano Energy* **2018**, *51*, 340−348.

DOI: 10.1021/acs.chemmater.9b02356
Chem. Mater. 2019, 31, 7565−7573